# Nanostructured Brownian Surfaces Prepared through Two-Photon Polymerization: Investigation of Stem Cell Response

**Attilio Marino,*,†,‡ Andrea Desii,*,† Mario Pellegrino,§ Monica Pellegrini,⊥ Carlo Filippeschi,† Barbara Mazzolai,† Virgilio Mattoli,*,† and Gianni Ciofani*,†**

†Center for Micro-BioRobotics, Istituto Italiano di Tecnologia, Viale Rinaldo Piaggio 34, 56025 Pontedera, Pisa, Italy, ‡The Biorobotics Institute, Scuola Superiore Sant'Anna, Viale Rinaldo Piaggio 34, 56025 Pontedera, Pisa, Italy, §Dipartimento di Ricerca Traslazionale e delle Nuove Tecnologie in Medicina e Chirurgia University of Pisa, Via Savi 10, 56126 Pisa, Pisa, Italy, and ⊥Scuola Normale Superiore di Pisa, Piazza dei Cavalieri 7, 56126 Pisa, Pisa, Italy

**ABSTRACT** Nondeterministic phenomena are at the base of plenty of biological processes that comprise physiological signaling, cellular communications, and biological architectures. Among them, natural surface topographies are often characterized by "chaotic" features that are not trivial to be recreated *in vitro*. Recently, some methods have been proposed to resemble the hierarchical organization of the extracellular microenvironment, through the chemical preparation of randomly rough and self-affine fractal surfaces. Notwithstanding, this approach does not allow the fractal dimension to be modulated at a desired value, being moreover the self-affinity maintained just for one decade of spatial frequencies. Here, we propose the replication of *in silico* generated Brownian surfaces through a



two-photon polymerization technique. As a result of the direct laser writing of the desired patterns, we were able to obtain highly reproducible self-affine (in a range of two spatial frequency decades) structures characterized by the desired predetermined Hurst exponents. Rat mesenchymal stem cells were moreover cultured on the obtained substrates, highlighting interesting phenomena concerning cell adhesion, cytoskeleton conformation, and actin polymerization, strictly depending on the fractal dimension of the surfaces.
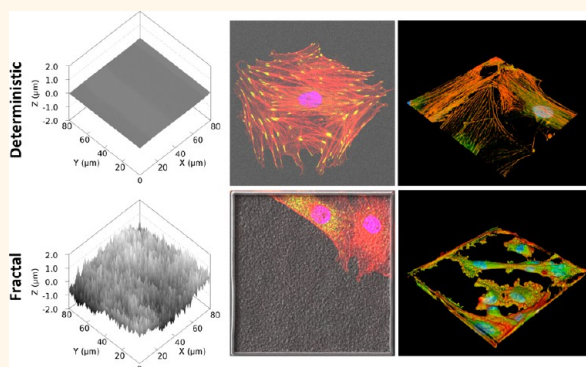
**KEYWORDS:** two-photon polymerization · bio/non-bio interfaces · Brownian surfaces · mesenchymal stem cells · cytoskeleton organization

Physical stimuli are well-known to strongly contribute to the modulation and to the fostering of several cell responses and behaviors:[1,2] a number of *in vitro* investigations have taken advantage of mechanical and topographical cues to control different cellular functions, including cytoskeletal organization and cell adhesion,[3,4] proliferation,[5,6] differentiation,[7] and reprogramming.[8] Concerning topographical stimuli, the effects of different surface features on the cell behavior have been intensively investigated: from these studies it has been found as cells are responsive to a wide range of surface topography sizes, from the micrometric to the nanometric scale.[9−13] Most of the exploited approaches have used discrete and ordered topographical stimuli, such as pillars, ridges and grooves,[14−17] but despite the biomimicry of some of these structures, natural surface topographies of extracellular matrix are often characterized by nondeterministic features and are organized over multiple scale ranges.[18]

A recent review pointed out as fractals play a key-role in the design of biomimetic approaches in tissue engineering,[19] and the complexity of biostructures, that often show fractal features, should be taken into account in the realization of innovative biomaterials and medical devices. Several examples can be reported, where fractal geometries have been successfully exploited, including modeling of biomaterials with

* Address correspondence to
attilio.marino@iit.it,
andrea.desii@iit.it,
virgilio.mattoli@iit.it,
gianni.ciofani@iit.it.

biological and/or synthetic origins,[20] designing of cell-culture matrices or scaffolds,[21] and designing of microstructured implants for enhanced tissue repair.[22] Fractal geometries present scaling features and self-similarity useful to understand mechanisms of cell adhesion and interaction with the substrate, as described for human neuronal cells.[23]

Fractional Brownian surfaces have been developed with traditional microfabrication methods for the assessment of the effects of fractal dimension on cell dynamics, and more complex 3D constructs have taken advantage from the fractal features of their surfaces to enhance osteogenesis, eventually for *in vivo* applications.[24] Surface topography is fact determinant in fostering different cellular activities and, in the case of stem cells, also their differentiation:[25,26] the investigation of different fractal dimensions is therefore of particular importance, also in view of recent findings that highlighted how it could represent an optimal descriptor of substrate topography[27] even better that the more traditional roughness evaluation.

In this perspective, a hierarchical organization of the *in vitro* extracellular microenvironment has been obtained through the chemical preparation of randomly rough and self-affine fractal surfaces,[28] prepared on silicon wafers by electrochemical etching in a KOH solution. The results of this work revealed a remarkable effect of the surface fractal dimension on cell adhesion and proliferation. However, the chemical methods used to generate self-affine surfaces do not allow the fractal dimension to be easily modulated at a desired value, being instead *a posteriori* characterized. For this reason, the possibility to develop a different procedure able to finely tune the fractal features of the surfaces would allow deeper investigations of the surface fractal dimension effects on cell behaviors to be performed.

Among several nanofabrication techniques, the two photon polymerization (2pp) represents a photolithographic procedure enabling the preparation of 3D structures with a high spatial resolution, down to 100 nm.[29,30] In particular, this method exploits the two-photon absorption of femtosecond laser pulses to polymerize specific regions of dedicated photoresists. Several recent studies adopted 2pp for the preparation of structures able to foster different cell behaviors, aiming at tissue engineering and regenerative medicine purposes.[31] As an example, cable-like structures resulted able to promote stem cell homing;[6] furthermore, we have recently demonstrated as bioinspired trabecular-like structures fabricated through 2pp present the capability to deeply affect SaoS-2 bone-like cell morphology, to promote their exit from the cell cycle, and to enhance their osteogenic differentiation.[32] As a further example, flexible structures fabricated by 2pp resulted to be interesting tools for the study of the cell mechanobiology and, in particular, for the measurement of the forces exerted by cells.[16,33]

In this work, we propose the exploitation of 2pp for the preparation of nanostructured surfaces characterized by specific Hurst exponents ($H$), and to analyze the effects of these surfaces on stem cell adhesion and cytoskeleton organization. As a result of the multiscale properties of the fractal surfaces, it has been possible to study the spatial frequencies able to elicit specific stem cell responses: we have prepared and characterized nanostructured surfaces presenting a wide range of different fractal features, such as deterministic, persistent, Brownian, and antipersistent, and we investigated the effects of these features on adhesion, cytoskeleton conformation, and membrane stiffness of rat mesenchymal stem cells (MSCs).

## RESULTS

**Brownian Surfaces Characterization.** Brownian surfaces characterized by different $H$ exponents have been obtained through a 2pp approach, as described in details in the Methods section, and as schematized in Figure 1. Video S1, supplied as Supporting Information, further describes the proposed innovative line-by-line fabrication process.

The design and the atomic force microscopy (AFM) characterization of the surfaces are reported in Figure 2. Starting from the left, the first column shows the synthetic height maps generated through the Gwyddion software, jointly to the nominal $H$ exponents. In the second column, the 3D rendering of AFM scans related to the actual surfaces obtained through 2pp technique are shown, jointly to their actual $H$ exponents. In the third column, we depict the top view of the half left side of synthetic height maps and the half right side of the polymerized surfaces, separated by a dashed white line (scale bar = 20 $\mu$m). The fourth column shows the power spectral density function (PSDF) analysis of the AFM scan relative to the different surfaces that allowed the $H$ exponents to be calculated owing to a fitting of the linear portion of the curve (see Methods for details). Briefly, the region of the PSDFs well described by a linear fitting on the log−log plot is depicted in green: the surface spatial frequencies in this range are considered self-affine, thus resulting in Brownian surfaces prepared through 2pp self-affine between 0.1 and 10 $\mu$m$^{-1}$.

As we can appreciate from the whole characterization and analysis, 2pp resulted an efficient technique able to accurately reproduce the features *in silico* generated by the software. With this approach, we were able to obtain surfaces in a wide range of different fractal features, characterized by different preimposed Hurst exponents (deterministic, $H = 1.00$; persistent, $H = 0.61$; properly Brownian, $H = 0.54$; antipersistent $H = 0.33$ and $H = 0.01$),[34] and self-affine in a range of two spatial frequency decades (0.1−10 $\mu$m$^{-1}$).

**Cell Response.** Different $H$ values did not significantly affect cell densities on the substrates, resulting of
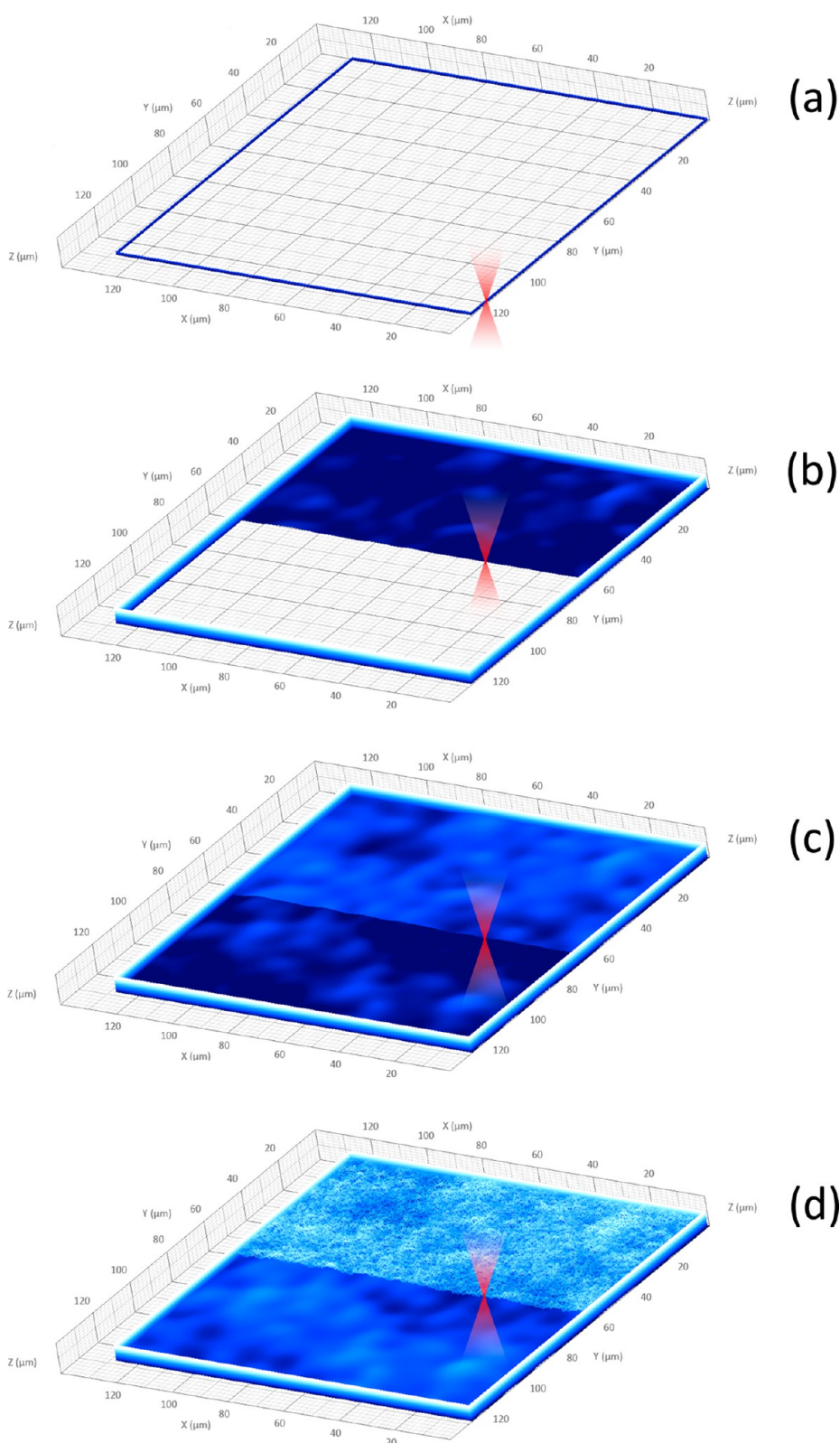
**Figure 1. Schematization of the fabrication process of the Brownian surfaces.** Each structure has been fabricated first by writing a square box of 128 $\mu$m × 128 $\mu$m acting as a scaffold (a), then two low-pass filtered surfaces (b and c) were written from the bottom-up, one line at a time, to give a reliable mechanical support to the final fractal surface (d).

about 20 000 cells/cm$^2$ for all of the surfaces at the end of each experiment (25 100 ± 5500 cells/cm$^2$ for the nominally flat surfaces, $H$ = 1.00; 25 000 ± 5100 cells/cm$^2$ for $H$ = 0.61 surfaces; 23 200 ± 5500 cells/cm$^2$ for $H$ = 0.54 surfaces; 21 400 ± 5600 cells/cm$^2$ for $H$ = 0.33 surfaces; 20 000 ± 5100 cells/cm$^2$ for $H$ = 0.01
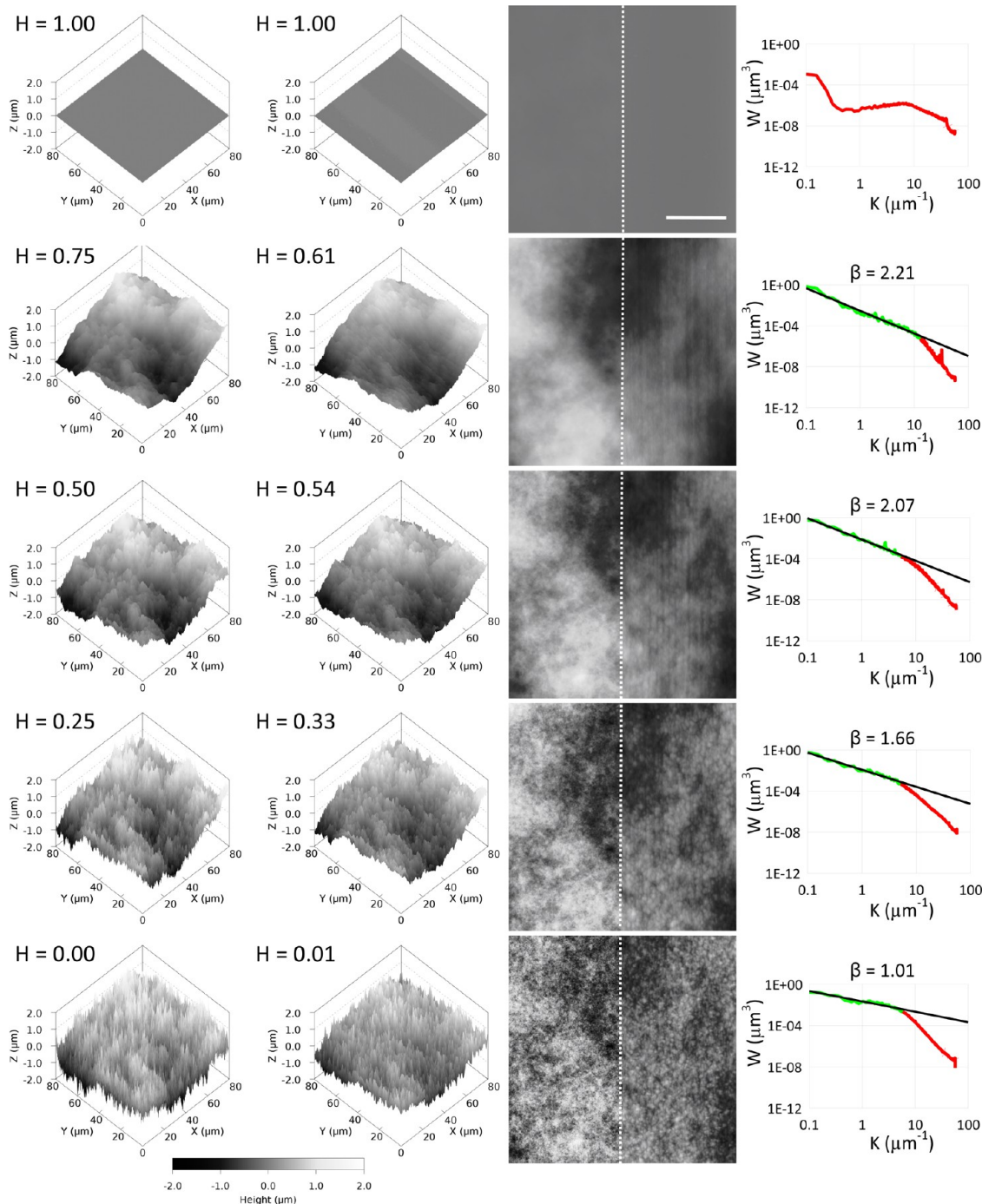
**Figure 2.** Brownian surface design and AFM characterization of the two-photon polymerized surfaces, characterized by different *H* exponents. Starting from the left: in the first column, the synthetic height maps generated through Gwyddion software; in the second column, the 3D rendering of AFM scan related to the different surfaces fabricated through two-photon polymerization technique (for each structure, the respective *H* exponent is indicated); in the third column, the top view of the half left side of synthetic height maps and the half right side of the fabricated surfaces AFM scan, separated by a dashed white line, scale bar = 20 $\mu$m; in the fourth column, power spectral density function (PSDF) analysis of the AFM scan relative to the different surfaces. In green, the region of the PSDF linearly fitted (in black); in red, the region of the PSDF not linear in the log−log plot.

surfaces; Kruskal−Wallis test *p*-value >0.05). Furthermore, we investigated the expression of the cell surface protein CD54, a typical stemness marker for mesenchymal cells,[35] on MSCs grown on the different surface conditions. We highlighted that all the investigated cells (*n* > 50 for each substrate) were positive for this marker,

on each typology of surfaces, as we can also appreciate from Figure S1 (Supporting Information).

To analyze the cytoskeleton response to the different Brownian surfaces, f-actin and vinculin expression patterns were deeply investigated through immunocytochemistry (ICC) followed by confocal microscopy
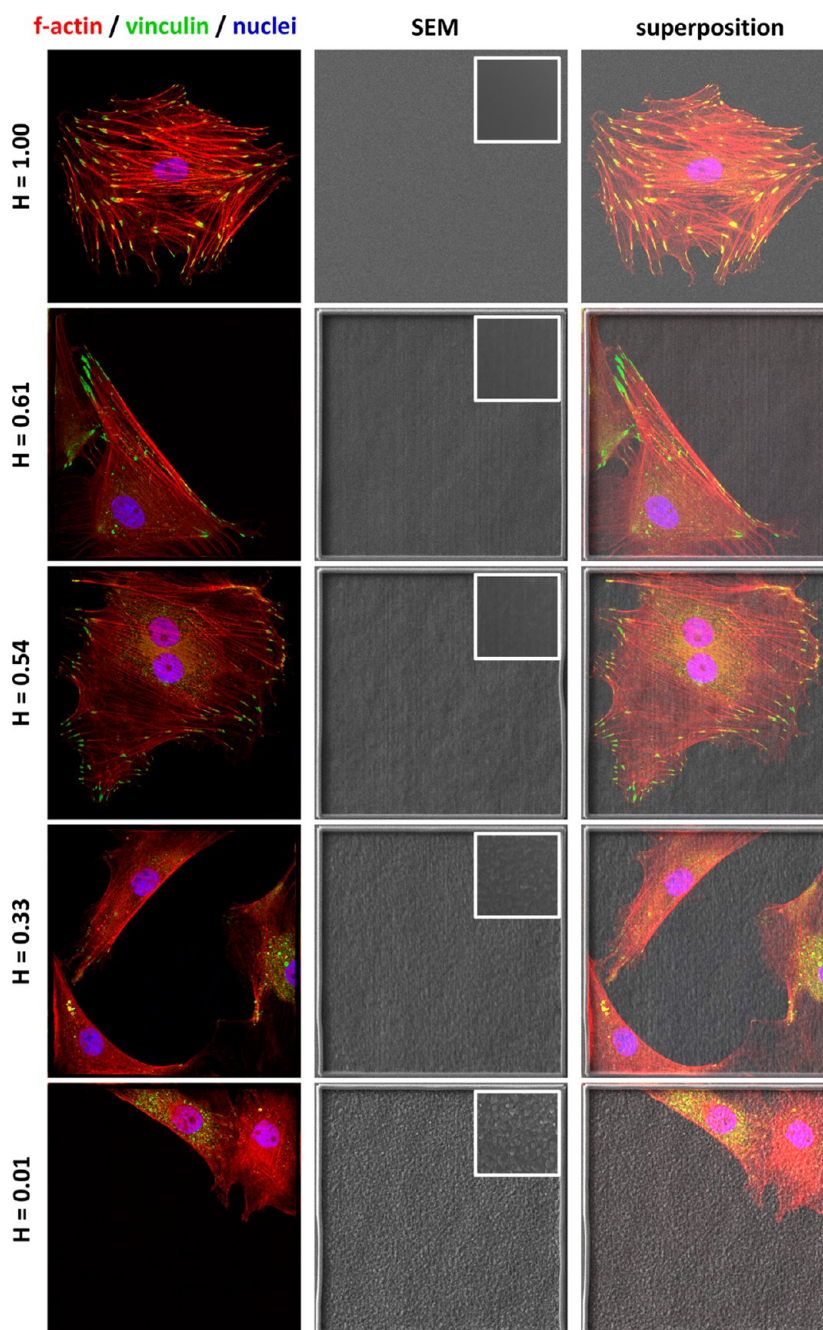
**Figure 3. Vinculin and f-actin organization in MSCs grown on surfaces characterized by different *H* exponents. In the left column, fluorescence confocal acquisitions of MSCs (in green, vinculin; in red, f-actin; in blue, nuclei); in the middle column, SEM images of the surfaces used for MSC cultures, in the box inset of each SEM acquisition, a high-magnification (20 *μ*m × 20 *μ*m) image is reported; in the right column, the superposition of the confocal and SEM acquisitions, scan area is 130 *μ*m × 130 *μ*m.**

(Figure 3). The first column of Figure 3 shows the f-actin (red) and the vinculin (green) expression in MSCs plated on the fractal surfaces. Qualitatively, it is possible to observe an important variation of the cytoskeleton organization. In particular, the f-actin of MSCs adhering on flat control and high-*H* surfaces is organized in well-defined stress fibers, while the f-actin expression was found to be homogeneously spread throughout the whole cell bodies in cultures performed on the low-*H* surfaces. Moreover, the expression pattern of

the vinculin, a cytoskeletal protein typical of the focal adhesion plaque, was differently organized among the investigated surfaces. Concerning flat control and high-*H* surfaces, vinculin is clustered at the distal region of the f-actin stress fibers, where the stress fibers are anchored to the cell membrane through the intracellular complex of the focal adhesion.[36] Instead, the vinculin in cells grown on low-*H* surfaces presents a different behavior, being not possible to observe the typical vinculin expression
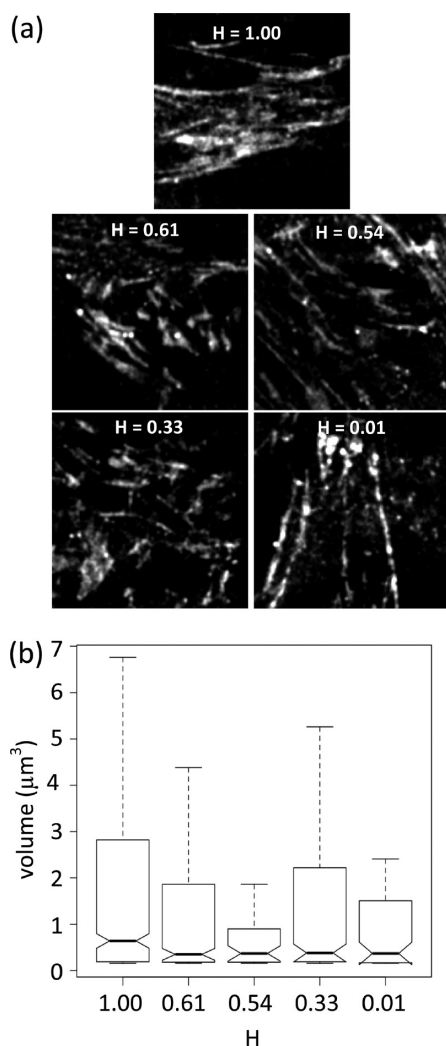
(a)



(b)

(c)
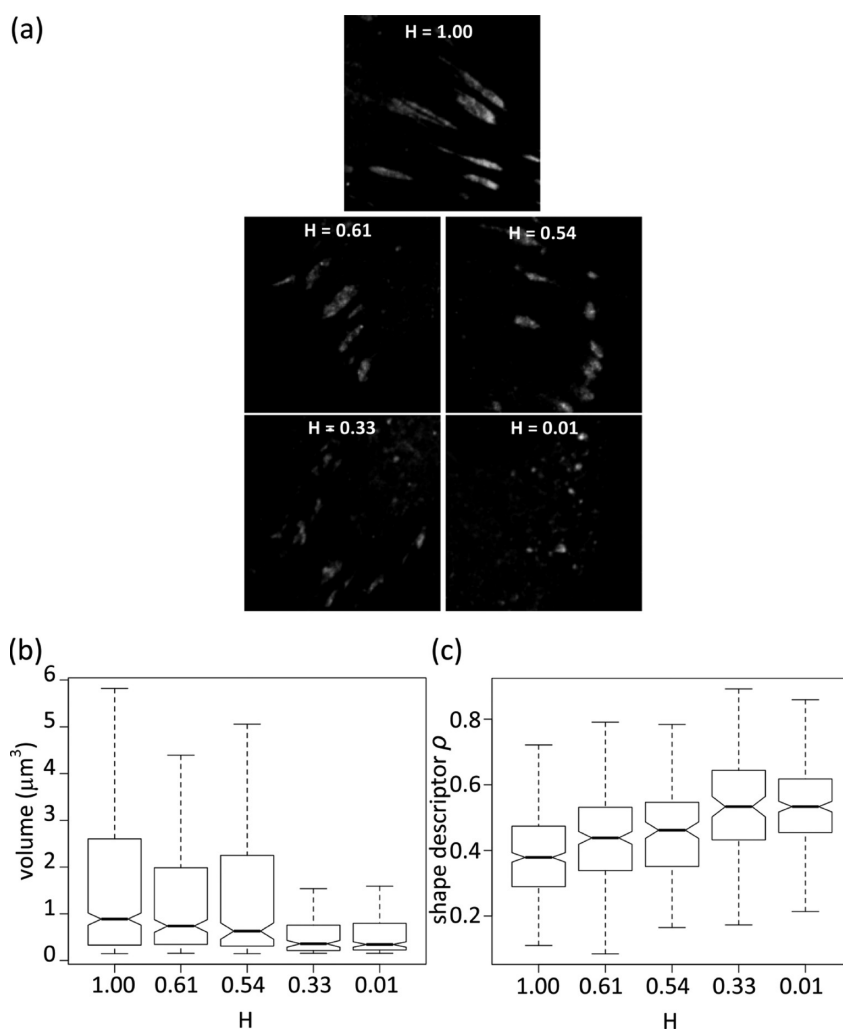


**Figure 4. Surface *H* exponent affects the vinculin clustering in MSCs. (a) High magnifications of the vinculin pattern expression of MSCs cultured on surfaces characterized by different *H* values (from *H* = 1.00 to *H* = 0.01), scan area is 20 $\mu$m $\times$ 20 $\mu$m. (b) Volume and shape descriptor $\rho$ distributions of MSC vinculin clusters maturated on different surface conditions; *p*-values related to all of the possible comparisons among distributions are available in Table S1 of Supporting Information.**

pattern: smaller and disorganized vinculin spots can be in fact appreciated from the confocal images, not localized in the cortical regions of the cells, but rather expressed in the perinuclear area. Furthermore, it is possible to observe that some cells growing on these surfaces (*H* = 0.33, *H* = 0.01) present a considerable reduction of vinculin expression, in terms of fluorescence signal intensity.

Scanning electron microscopy (SEM) imaging of flat and fractal surfaces are reported in the second column of Figure 3. A magnification of the respective surface scan is shown in the inset at the top-right of each SEM image. Similarly to observations performed following AFM analysis, low-*H* substrates (*H* = 0.01 and *H* = 0.33) were characterized by a relatively jagged surface with respect to the high-*H* substrates (*H* = 0.54 and *H* = 0.61) and to the nominally flat surface (*H* = 1.00). The third column of Figure 3 represents the superposition of ICC images and the SEM scans of the corresponding substrate.

A deeper, quantitative, analysis of vinculin and f-actin expression is reported in the following.

High magnifications of the vinculin expression patterns in cells cultured on the fractal and flat substrates are reported in Figure 4a. Aiming at a quantitative analysis, volume and shape measurements of the vinculin clusters were performed. We observed a gradual decrease of the vinculin cluster volume when *H* is decreasing (0.89 $\pm$ 0.13 $\mu$m$^3$ for the nominally flat surfaces, *H* = 1.00; 0.74 $\pm$ 0.14 $\mu$m$^3$ for *H* = 0.61 surfaces; 0.63 $\pm$ 0.17 $\mu$m$^3$ for *H* = 0.54 surfaces; 0.36 $\pm$ 0.07 $\mu$m$^3$ for *H* = 0.33 surfaces; 0.34 $\pm$ 0.06 $\mu$m$^3$ for *H* = 0.01 surfaces; Figure 4b; Kruskal−Wallis test *p*-value < 0.05; *p*-values of Nemenyi−Damico−Wolfe−Dunn posthoc test are available in Table S1 of Supporting Information). Moreover, our analysis revealed a significant effect of the surface fractal features on the shape of vinculin expression, in terms of variation of the $\rho$ parameter, defined in eq 2 (0 < $\rho$ < 1, being $\rho$ = 1 for a sphere). In particular, the vinculin clusters detected

(a)



(b)



**Figure 5. Effects of the surface *H* exponent on integrin patterns in MSCs. (a) High magnifications of the integrin pattern expression of MSCs cultured on surfaces characterized by different *H* value (from *H* = 1.00 to *H* = 0.01), scan area is 20 $\mu$m × 20 $\mu$m. (b) Volume distributions of MSC integrin clusters for different surface conditions; *p*-values related to all of the possible comparisons among distributions are available in Table S1 of Supporting Information.**

on low-*H* substrates were characterized by a rounded shape (0.53 ± 0.02 for *H* = 0.01 surfaces; 0.53 ± 0.03 for *H* = 0.33 surfaces), while the shape of those observed on flat and high-*H* surfaces was significantly more elongated (0.46 ± 0.03 for *H* = 0.54 surfaces; 0.44 ± 0.03 for *H* = 0.61 surfaces; 0.38 ± 0.01 for *H* = 1.00 surfaces; Figure 4c; Kruskal−Wallis test *p*-value <0.05; *p*-values of Nemenyi-Damico-Wolfe-Dunn post-hoc test are available in Table S1 of Supporting Information).

To investigate whether the observed variation of the vinculin clustering on the different surface conditions is due to a change in size of the cell−substrate adhesions, the integrin expression pattern has been investigated (Figure 5a). Indeed, the integrin pattern expression, differently from the vinculin clustering, reveals that the entire binding site of the focal

adhesions to the substrate does not vary depending on the f-actin conformation (please see in the following for details) and, therefore, on the tension/stretch applied at the focal adhesions.[37] Differently from the results concerning vinculin, it was not possible to detect a significant difference in terms of integrin clustering in the cells grown on the different substrates, except for the nominally flat surface condition, where a higher volume of the integrin clusters was revealed (0.64 ± 0.16 $\mu$m$^3$ for nominally flat surfaces, *H* = 1.00; 0.35 ± 0.13 $\mu$m$^3$ for *H* = 0.61 surfaces; 0.37 ± 0.16 $\mu$m$^3$ for *H* = 0.54 surfaces; 0.38 ± 0.19 $\mu$m$^3$ for *H* = 0.33 surfaces; 0.37 ± 0.24 $\mu$m$^3$ for *H* = 0.01 surfaces; Figure 5b; *p*-values of Nemenyi−Damico−Wolfe−Dunn post-hoc test are available in Table S1 of Supporting Information).

Concerning the investigation of the f-actin organization, high magnifications of the f-actin expression patterns are depicted in the first column of Figure 6. In the box inset of each fluorescence acquisition, Fast Fourier Transform (FFT) image of the respective surface scan is reported. The analysis of the f-actin fluorescence intensity profile (plots in the second column of Figure 6) quantitatively shows a progressive decrease in the amplitude of the relative fluorescence signal peaks of the stress fibers, from the flat to the low-*H* surface conditions. Furthermore, the circular profile analysis of the FFT images relative to the f-actin acquisitions revealed a peak in the nominally flat surfaces, thus demonstrating a highly organized f-actin pattern in terms of well aligned stress fibers. This peak gradually decreases moving from high-*H* surfaces to low-*H* substrates, disappearing in cells cultured on surfaces with *H* = 0.01 (plots in the third column of Figure 6).

To evaluate whether the decrement of stress fiber formation in the low-*H* surface conditions could be ascribed to an alteration of the f-actin polymerization, the g-actin (globular, nonpolymerized actin) levels were investigated (Figure 7a). Interestingly, we observed a progressive increment of g-actin fluorescence signal intensity from flat to low-*H* surfaces (8.04 ± 0.54 for *H* = 1.00 surfaces; 9.14 ± 0.73 for *H* = 0.61 surfaces; 14.87 ± 1.41 for *H* = 0.54 surfaces; 16.24 ± 0.57 for *H* = 0.33 surfaces; 19.89 ± 1.08 for *H* = 0.01 surfaces; Figure 7b; Kruskal−Wallis test *p*-value < 0.05; *p*-values of Nemenyi−Damico−Wolfe−Dunn post-hoc test are available in Table S1 of Supporting Information). Figure S2 (in Supporting Information) depicts a panel showing confocal images of the expression of g-actin (left column) and f-actin (middle column) in all the considered situations, jointly to a 3D rendered reconstruction of the merged signals (right column).

The observed effects of the different substrates on the MSC cytoskeleton prompted us to investigate possible consequences on the cell stiffness. We used a noncontact method based on the ion conductance
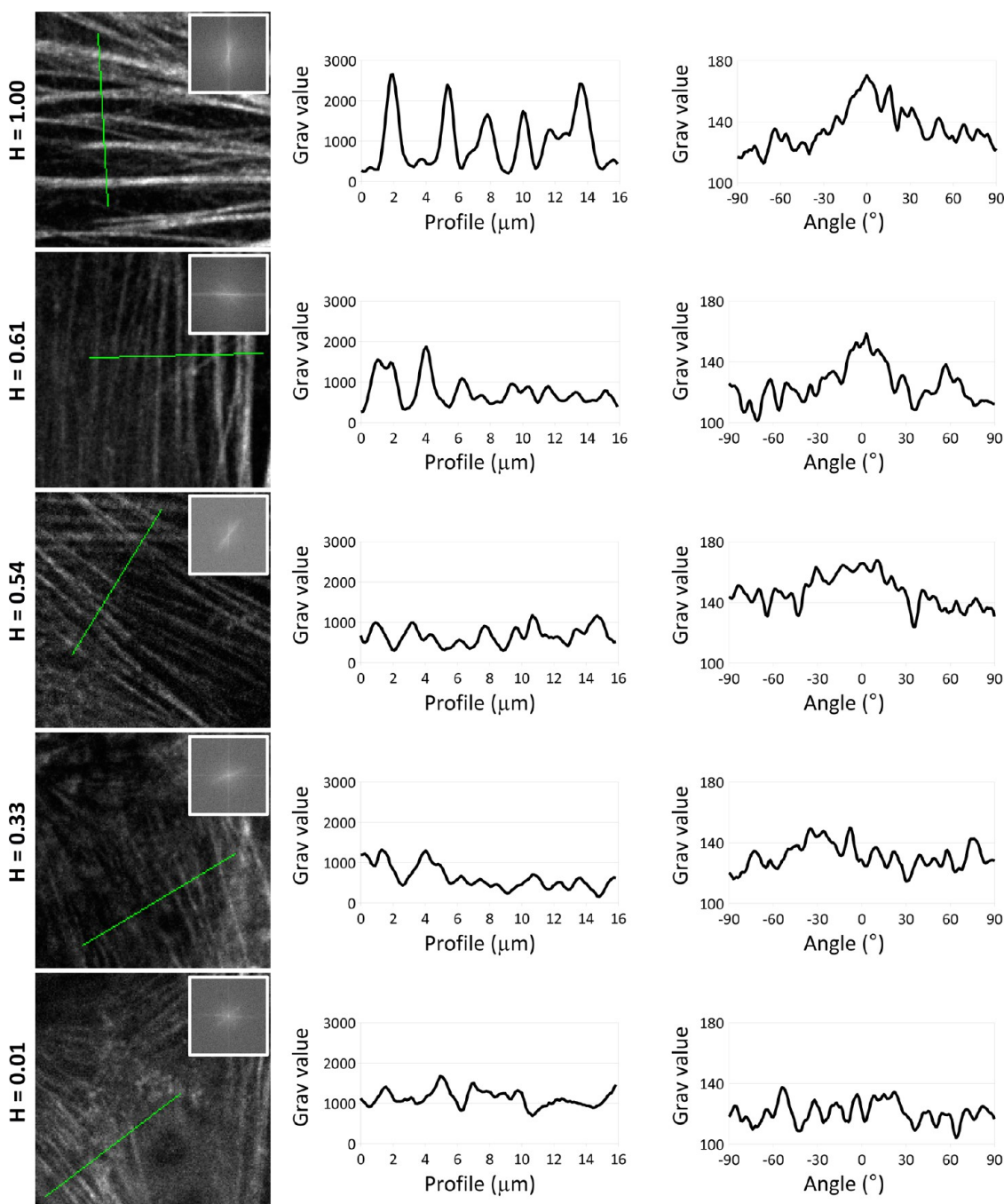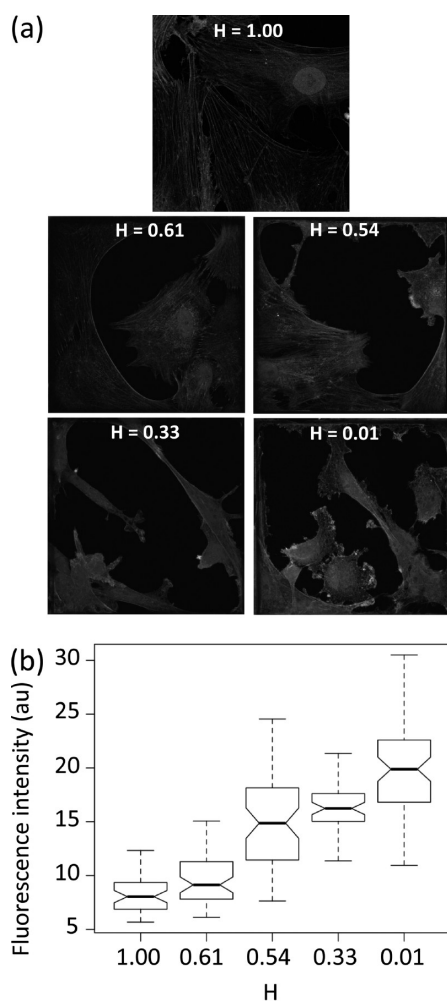
**Figure 6. Surface *H* exponent affects the stress fiber formation.** In the left column, high magnifications of the f-actin organization of MSCs cultured on surfaces characterized by different *H* values (from *H* = 1.00 to *H* = 0.01) are depicted, scan area is 20 $\mu$m $\times$ 20 $\mu$m; in the inset of each confocal fluorescence acquisition, the Fast Fourier Transform (FFT) image of the respective surface scan is reported; in the middle column, the analysis of the f-actin fluorescence intensity profile; in the right column, the circular profile analysis of the FFT images relative to the f-actin acquisitions.

scanning probe microscopy, as reported in details in the Methods section, to investigate cell mechanical properties. Figure 8a illustrates typical *I/Z* curves recorded when approaching to the glass or to the cells grown on substrates with different fractal dimension, with an applied pressure of 8 kPa. Ion current is normalized to its maximum value and $\delta$ indicates the difference in *Z* positions at $I/I_0$ of 0.99% and 0.98%. It can be observed that this value decrease with the

*H* value: more specifically, the mean values of elastic modulus measured in groups of cells plated on the different substrates are reported in Figure 8b. These data show a progressive reduction of MSC stiffness in response to an increment of the *H* exponent of the surface, well described by a linear relation (Ordinary Least Squares method) between the Young's modulus *E* and the *H* exponent, being $E = 1117.5H + 797.7$ ($R^2 = 0.98$).

(a)

H = 1.00

H = 0.61     H = 0.54

H = 0.33     H = 0.01

(b)



Figure 7. Surface $H$ exponent affects the g-actin levels in MSCs. (a) Confocal fluorescence acquisitions of g-actin expression in MSCs cultured on surfaces characterized by decreasing $H$ exponents, scan area is 130 $\mu$m $\times$ 130 $\mu$m. (b) Fluorescence intensity distributions of signal relative to the g-actin in different surface conditions; $p$-values related to all of the possible comparisons among distributions are available in Table S1 of Supporting Information.

## DISCUSSION

In this work, we have shown for the first time the preparation of self-affine nanostructured surfaces, characterized by imposed desired Hurst exponents, thanks to the 2pp technique. In particular, PSDF analysis of AFM scans demonstrated as we were able to fabricate different substrates, such as persistent, properly Brownian, and antipersistent surfaces, characterized by the desired predetermined $H$ exponent. Furthermore, the self-affinity, which is observed in the linear region of the log−log PSDF plot, was maintained for about two decades, that can be considered a particular wide range of spatial frequencies if compared to other results obtained through traditional chemical approaches, where it was instead maintained for just one decade.[28]

Analyzing the effects of deterministic and fractal surfaces on the MSC stemness, the CD54 expression
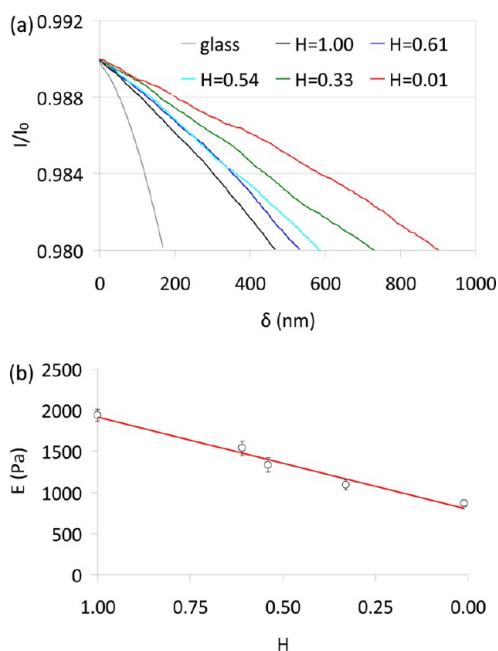


Figure 8. Surface $H$ exponent affects the cell membrane stiffness, which is measured thanks to scanning ion conductance microscopy (SICM). (a) Typical $I/Z$ curves recorded when approaching a SICM pipet with an applied pressure of 8 KPa to glass or to cells plated on different surface conditions (from $H$ = 1.00 to $H$ = 0.01); ion current is normalized to its maximum value and $\delta$ indicates the difference in $Z$ positions at $I/I_0$ = 0.99% and 0.98%: it can be observed as this value decreases along the $H$ value. (b) The mean values of elastic modulus $E$ measured in groups of cells plated on the different substrates are reported, showing a progressive and linear $E$ reduction in response to a decreased surface $H$ value.

was found qualitatively comparable over surfaces characterized by different $H$ exponents (0.01 < $H$ < 1.00). This finding differs from results obtained by applying other physical cues (*i.e.*, roughness and stiffness) that are instead well-known to affect cell stemness.[38,39]

Concerning MSC cytoskeleton organization, we noticed a gradual change from nominally flat conditions to highly fractal surfaces ($H$ = 0.01), involving vinculin, f-actin and g-actin expression. In particular, the increase of the surface fractal dimension is accompanied by a gradual disorganization of the actin stress fibers and by a reduction of the vinculin cluster size. Concerning stress fibers, their reduction observed on low-$H$ surfaces coincided with an increment of the nonpolymerized g-actin, thus indicating that the reduced stress fiber formation was not due to a decrease in the available g-actin pool but, rather, to a topography-dependent inhibition of actin polymerization. It is well demonstrated that several chemical stimuli are able to inhibit the stress fiber formation maintaining high g-actin levels.[40,41] However, at the best of our knowledge, the variation of g-/f-actin balancing into cells cultured on different surfaces was scarcely investigated. Obtained results are not obvious, because in most of living cells the g-actin content is usually maintained at a higher level than the critical concentration necessary for the actin filament polymerization,[42]

acting as a reservoir for stimulus-induced actin assembly.[43,44] Observed results suggest that the topographical stimulus given by our surfaces presents, as a consequence, an important alteration of the f-actin polymerization mechanisms, demonstrated by the increment of the available g-actin pool, significantly higher in cultures performed on low-*H* surfaces because of a hindered f-actin assembly.

Concerning vinculin expression pattern, the reduction of the vinculin aggregation at the focal adhesion plaques is likely related to a lower tension exerted at the level of the adhesion site. This hypothesis seems to be strengthened by the observation of a progressive disorganization of stress fibers in response to an increase of the fractal dimension. Indeed, it is widely recognized as the accumulation of vinculin molecules to the Vinculin Binding Sites (VBSs) of talin is force/stretch dependent,[45] and a reduction of actomyosin-based force at focal adhesion decreases the amount of vinculin in that region.[37] For example, treatment with blebbistatin, a myosin II inhibitor which destabilizes and disassembles stress fibers, induces a significant reduction of vinculin in several cell types.[46] However, not only do stress fibers guide the focal adhesions to maturity,[47] but also the stress fiber formation depends on the cell–substrate adhesion efficiency.[48] For this reason, another possible hypothesis should consider that the high-spatial frequencies present on the low-*H* surfaces could not allow for the formation of sufficiently large focal adhesions. To understand whether the increasing fractal features can affect the cytoskeleton organization by altering the focal adhesion formation, or directly by acting on the stress fibers, we analyzed the pattern expression of integrin. This protein constitutes the trans-membrane component of the focal adhesions, and its clustering has been proven in many cases to be independent of stress fiber destabilization.[37] The investigation of integrin clustering revealed a difference just among the nominally flat surfaces and all the other substrates, but no significant differences were detected among the fractal surfaces: the nominally flat surfaces allow for the formation of cell–substrate adhesions larger than those found on Brownian surfaces, but no significant differences in integrin cluster sizes occur when $0.01 \leq H \leq 0.61$. In these conditions, the significant decrease of the vinculin cluster sizes observed on low-*H* surfaces (when compared to high-*H* surfaces) cannot thus be ascribed to the formation of smaller focal adhesions. Instead, the reduction of the vinculin clustering, which is known to occurs depending on the tension applied by stress fibers to the talin molecules of focal adhesions,[37] is reasonably caused by the actin fiber disorganization induced by the increment of the surface fractal features.

It is well-known that the formations of focal adhesions and stress fibers are dynamic and synergistic phenomena,[49,50] which allow the cell to assume a definite shape and to maintain a certain tension.[51] The observed changes in the distribution of vinculin in the focal adhesion complexes and of the f-actin stress fibers are potentially able to alter both the cellular biochemistry and mechanics. According to the mechanical model of cell structure based on tensegrity architecture,[51] a significant alteration in the pattern of cellular stress distribution is expected to affect the tension of the whole cell surface: for this reason, the membrane elasticity of MSCs adhering on different substrates was investigated. Since MSCs on high-*H* surfaces were able to develop mature focal adhesions even in distal regions of cellular body, and to polymerize actin in well-organized stress fibers, an increased cell rigidity was expected. Consistently with our hypothesis, the results showed a significant and progressive reduction of membrane stiffness in response to the *H* decrement of the nanostructured surfaces. This experimental evidence is particularly interesting because not only cell adhesion, but also membrane tension is able to affect several different biochemical phenomena,[52] and also to regulate fundamental functions such as vesicular trafficking and cell migration.[53]

All the collected results assume particular significance in view of the effects of cytoskeleton modifications on stem cells proliferation and differentiation. It has been proven, for example, that an actin–myosin generated tension is mandatory for the activation of the RhoA-ROCK commitment signaling in osteogenic differentiation of human MSCs,[54] demonstrating that cytoskeleton conformation and tension play a key role in determining stem cell fate. In another work, cytoskeleton was modulated by using different depolymerising (cytochalasin D, latrunculin A) and stabilizing (jasplakinolide) drugs, showing that the modulation of the cytoskeleton can influence both integrin-mediated mechanically induced signaling pathways and stem cell differentiation.[55] Cytoskeleton conformation can be moreover used as a "predictor" of stem cell fate, by using appropriate analysis of actin patterns, such as shapes, intensities, textures, and spatial distributions.[56]

It is therefore clear that observed phenomena on fractal surfaces could be exploited, in the future, to help the commitment of stem cells toward specific lineages. Different *H*-values are in fact able to elicit different vinculin patterns, cytoskeleton conformation, and, consequently, cell stiffness, thus representing a further biomechanical cue able to modulate stem cell fate.[57] Of course, deeper investigations of MSC commitment will be necessary to assess the actual effects of the proposed Brownian substrates on the differentiation processes.

## CONCLUSION

In this paper, we have proposed the preparation of nanostructured surfaces characterized by different fractal features, in terms of Hurst exponents, owing to an innovative approach based on a line-by-line and

multilayer fabrication of substrates through two-photon direct laser writing. This technique allowed highly reproducible substrates to be prepared, with well-defined pre-determined self-affine characteristics ($H = 0.01-1.00$) in the range of two spatial frequency decades ($0.1-10~\mu m^{-1}$). Testing on mesenchymal stem cells revealed significant effects of the fractality on cell adhesion (in terms of vinculin pattern maturation), on cytoskeleton conformation (in terms of actin polymerization and organization) and, as a consequence, on cell mechanical properties (in terms of cellular stiffness).

In our opinion, obtained results are extremely important under both a technological and a biological point of view. This is in fact the first example of nanofabricated fractal geometries with *a priori* tunable features obtained through a physical approach. Moreover, investigation of stem cells/nanotopography interactions allowed significant information about cellular response to complex surface cues to be obtained, giving important suggestions for the development of innovative materials and scaffolds for cellular and regenerative therapies.

## METHODS

**Surface Design, Preparation, and Characterization.** Brownian height maps were generated with the spectral synthesis module of Gwyddion, a scanning probe microscopy (SPM) analysis software,[58] using the Fourier filtering method (http://gwyddion. net/features.php). The size of each map was 128 $\mu$m × 128 $\mu$m with a resolution of 200 nm and a RMS roughness of 0.5 $\mu$m, while the Hurst exponent, related to the fractal dimension of the maps, was chosen between 0 and 0.75. All generation processes were carried out with the same random seed. Low-pass filtered versions of the maps, used for the fabrication of two supporting layers of the Brownian surfaces, were obtained by 2D FFT filtering with Gwyddion. Height values of the filtered maps were offset by 1 $\mu$m. The resulting matrices of values were converted to files with instructions for the Direct Laser Writing (DLW) system using a Scilab function (Scilab Enterprises, http://www.scilab.org).

To fabricate the Brownian surfaces characterized by an increasing Hurst exponent, the two-photon polymerization (2pp) technique was performed with a DLW system (Photonic Professional, Nanoscribe GmbH) as described elsewhere.[16] Briefly, the biocompatible and well-characterized photoresist Ormocomp was cured on glass coverslips using a 100× objective (numerical aperture = 1.4) mounted on an inverted microscope (Zeiss), a laser power of 5 mW, and a scan speed of about 50 $\mu$m/s. A photon wavelength of 790 nm and a pulse duration of 120 fs were used. Each structure was fabricated first by writing a square box of 128 $\mu$m × 128 $\mu$m acting as a scaffold (Figure 1a); then surfaces were written according to the instruction files obtained from the synthesized height maps. Two low-pass filtered offset surfaces supporting the Brownian surface (Figures 1b,c) were written from the bottom-up, one line at a time, to give a reliable mechanical support to the final surface (Figure 1d) owning the described fractal features. A video depicting the whole procedure is also reported as Supporting Information (Video S1).

A triplicate of all the different Brownian surfaces were fabricated, thus generating a "chip" of nanostructured substrates on a single glass coverslip (Supporting Information Figure S3). Subsequently, samples were treated for 7 s with the Ormodev developer (Micro Resist Technology) in order to remove the nonpolymerized resist, washed in isopropyl alcohol, and eventually rinsed in ethanol.

The substrates were characterized through atomic force microscopy (AFM, Innova SPM, Bruker), operating in tapping mode using n-type silicon probes (NSG10 $f_0 = 140-390$ kHz, $k = 3.1-37$ N m$^{-1}$, NT-MDT). Surface topology was evaluated on 80 $\mu$m × 80 $\mu$m scans centered on the sample center, recorded at 0.5 Hz. For each sample, scan data were leveled to remove sample tilt, and the radial power spectral density function (PSDF) was calculated using Gwyddion and compared with the PSDF of the corresponding synthesized height map. Hurst exponent was calculated by regression (Ordinary Least Squares method) on the log−log plot of the linear portion of the PSDF, with the slope $\beta$ of the fitted line related to the Hurst exponent through following equation:[59−62]

$$\beta = 2H + 1 \qquad (1)$$

3D plots of surfaces were created with Gnuplot (http://www. gnuplot.info/).

Scanning electron microscopy (SEM) imaging (Helios Nano-Lab 600i FIB/SEM, FEI) was carried out on samples previously gold-sputtered for 25 s at 60 nA, obtaining a 3 nm thick conductive layer.

**Cell Cultures and Biological Staining.** Rat mesenchymal stem cells (MSCs, PT2505 from Lonza) were used in order to investigate the fractal dimension effects of different nanostructured surfaces on cell adhesion and on cytoskeleton organization. Cells were maintained in T-75 flasks using phenol-red free Dulbecco's modified Eagle medium (DMEM) supplemented with 10% fetal bovine serum (FBS), 2 mM L-glutamine, 100 U/mL penicillin and 100 $\mu$g/mL streptomycin. Medium was changed every 3−4 days and cells were split every 7 days using trypsin 0.05% with 0.02% EDTA. For the nanostructured surface testing, MSCs were plated at a density of 10 000 cells/cm$^2$ on the coverslips presenting the chip, without any previous coating.

For the analysis of the cytoskeleton organization, cells were fixed (4% paraformaldehyde in PBS at 4 °C for 20 min) 36 h after plating. Vinculin, an intracellular component of the focal adhesion complex, was stained by standard immunocytochemistry protocol. A primary mouse IgG anti-vinculin antibody (1:50 dilution in 10% goat serum, 90227 from Millipore), and a secondary goat FITC-IgG anti-mouse (1:50 in 10% goat serum, AP124F from Millipore) were used. Integrin, a trans-membrane protein component of focal adhesions, was revealed with a primary rabbit IgG anti-integrin α5 antibody (1:100 dilution in 10% goat serum, AB1928 from Millipore) and a secondary goat TRITC-IgG anti-rabbit (1:250 in 10% goat serum, A16101 from Life Technologies). CD54 (a positive marker for rat MSCs) staining was performed with the same immunocytochemistry procedure, using a primary mouse IgG anti-CD54 antibody (1:100 dilution in 10% goat serum, MAB2130 from Millipore) and a secondary goat FITC-IgG anti-mouse (1:50 in 10% goat serum, AP124F from Millipore).

Cytoskeletal g-actin, f-actin, and cell nucleus staining was performed by incubating cells with Alexa Fluor 488-conjugated DNaseI (D12371 from Invitrogen), TRITC-conjugated phalloidin (90228 from Millipore) and DAPI (90229 from Millipore), respectively, following standard procedures.

**Image Acquisition and analysis.** The 3D organization of vinculin, integrin, g-actin, and f-actin was investigated through a layer by layer scanning at high resolution thanks to confocal laser fluorescence microscopy (C2s confocal microscope, Nikon). In particular, a 60× oil-immersed objective was used to acquire z-stacks at a distance of 125 nm. Laser and photomultiplier settings were maintained constant during all the acquisitions. The image analysis were performed by using ImageJ software (http://rsbweb.nih.gov/ij/).

Vinculin expression patterns were automatically detected through the 3D boundaries of the clusters. Their shape was analyzed by using the 3D ImageJ Suite (ImageJ).[51] More specifically, the 3D Object Counter allowed the 3D selection and volume measurements of the vinculin clusters to be performed. Thereafter, the ellipsoid fitting of the clusters was carried out by

using the 3D Ellipsoid Fitting plug-in (Supporting Information Figure S4).[63] The geometric mean $\rho$ of the roundness of the two elliptical projections that univocally describe the ellipsoid was adopted as shape descriptor for comparing the 3D morphology of the vinculin clusters matured on different nanostructured surfaces, calculated according to eq 2:

$$\rho = \sqrt{a_1 a_2} = \sqrt{\frac{r_1}{r_2} \frac{r_1}{r_3}} = \frac{r_1}{\sqrt{r_2 r_3}} \qquad (2)$$

where $a_1 = (r_1/r_2)$ and $a_2 = (r_1/r_3)$ are the roundness of the elliptical projections on the $xz$ and $xy$ planes, respectively, and $r_1 < r_2 < r_3$ (see Supporting Information Figure S4d for further details).

A similar procedure was adopted for the analysis of the volume of the integrin clusters.

Organization of cytoskeleton f-actin was investigated by plotting the fluorescence intensity along a straight line selection of about 16 $\mu$m, perpendicular to the stress fiber main axis. Moreover, the intensity profile of a circular selection around the center of the Fast Fourier Transform (FFT) of the images reporting actin filaments organization was obtained with the Oval Profile plug-in (ImageJ).

Finally, in order to compare the g-actin expression of MSCs grown on different surfaces, more than 50 regions of interest (ROI) of about 400 $\mu$m$^2$ were considered for each condition, and the average fluorescence intensity of each ROI was sampled.

**Scanning Ion Conductance Microscopy and Cell Mechanical Properties.** The mechanical stiffness of living cells cultured on the substrates presenting different fractal dimensions was measured by using a scanning ion conductance microscope (SICM).

Pipettes with an opening radius of about 200 nm were made from borosilicate glass capillaries (1B100F-4, WPI) using a Mecanex BB-CH puller. An Ag−AgCl wire was used as reference, connected to the bath through a saline agar bridge, while an active Ag−AgCl electrode was immersed in the pipet solution. The pipet, inserted in a patch-clamp holder, was mounted on a piezo-translator stage (Nanocube P-611 3S with a driver E-664, Physik Instrumente). A syringe controlled by a micrometric screw applied a given pressure ($\Delta P$) both to the pipet holder and to a pressure transducer (Fujikura). The signals were low-pass filtered at 400 Hz. Two data acquisition cards (PCI-6251, National Instruments) were used for the digital-to-analog control of the piezo-driver and for the analog-to-digital acquisition, at 1 kHz, of ion current, pressure transducer, and position sensor signals. The software for both the scan control and the online data analysis has been developed in LabVIEW 8.2.1. For the positioning of the pipet, SICM was mounted on the stage of an inverted microscope (Nikon Diaphot 300) equipped with a 40× objective (0.55 N.A.PH3, Nikon).

When a SICM pipet approaches a sample along the $Z$ axis, the current decreases because of the reduction of the conducting space. The pipet can be stopped when the ion current ($I$) is reduced to a preset percentage of its maximum value ($I_0$), initially measured far from the sample. An external hydrostatic pressure ($\Delta P$) can be applied at the pipet aperture to determine a solution flow; consequently, the force exerted by the flow progressively induces a displacement of the target. Thus, the probe has to approach for an additional distance to decrease $I/I_0$ to the same defined preset threshold. The target displacement just before the contact can be indirectly obtained by analyzing two $I/I_0$ vs pipet displacement curves recorded with and without the application of the pressure.[64,65] At a given pressure, the current drops at smaller rates on softer samples. As recently reported, cell deformations can also be obtained at a single given pressure, taking as reference the infinitely stiff substrate, such as glass.[66]

Three to five cells *per* experimental condition were analyzed, and $I/Z$ curves were recorded at 16 different points of each cell, sequentially applying five different pressure values, in the range 0−12 k Pa. Local elastic modulus was determined by recording the ion current as a function of the vertical pipet position ($I/Z$ curve), with a 8 kPa constant pressure applied to the pipet. The data set was processed with both of the described methods, with consistent results.

**Statistical Analysis.** All the described experiments were carried out in triplicate, the normality of all the data distributions were tested with the Shapiro normality test, and subsequently, the nonparametric Kruskal−Wallis test was performed in order to compare the different distributions. Nemenyi−Damico−Wolfe−Dunn post-hoc test was used in order to compare all the single distributions. Finally, data were shown on box-plots and were expressed as median ± 95% confidence interval.

*Conflict of Interest:* The authors declare no competing financial interest.

*Supporting Information Available:* Four figures, one table, and one video. Figure S1 shows the CD54 stemness marker expression in MSCs grown on different surface conditions. Figure S2 reports f-actin, g-actin, and merged images of acquisitions of cells cultured on the different substrates. Figure S3 shows the design and an actual image of the chip used for biological experiments. Figure S4 depicts the procedure of image segmentation for vinculin pattern analysis. Table S1 summarizes results of statistical analysis performed in this work. Video S1 describes the line-by-line fabrication process. This material is available free of charge *via* the Internet at http://pubs.acs.org.

## REFERENCES AND NOTES

1. Keung, A. J.; Kumar, S.; Schaffer, D. V. Presentation Counts: Microenvironmental Regulation of Stem Cells by Biophysical and Material Cues. *Annu. Rev. Cell Dev. Biol.* **2010**, *26*, 533–556.

2. Nikukar, H.; Reid, S.; Tsimbouri, P. M.; Riehle, M. O.; Curtis, A. S. G.; Dalby, M. J. Osteogenesis of Mesenchymal Stem Cells by Nanoscale Mechanotransduction. *ACS Nano* **2013**, *7*, 2758–2767.

3. Seo, C. H.; Furukawa, K.; Montagne, K.; Jeong, H.; Ushida, T. The Effect of Substrate Microtopography on Focal Adhesion Maturation and Actin Organization *via* the RhoA/ROCK Pathway. *Biomaterials* **2011**, *32*, 9568–9575.

4. Seo, C. H.; Jeong, H.; Furukawa, K. S.; Suzuki, Y.; Ushida, T. The Switching of Focal Adhesion Maturation Sites and Actin Filament Activation for MSCs by Topography of Well-Defined Micropatterned Surfaces. *Biomaterials* **2013**, *34*, 1764–1771.

5. Thakar, R. G.; Chown, M. G.; Patel, A.; Peng, L.; Kumar, S.; Desai, T. A. Contractility-Dependent Modulation of Cell Proliferation and Adhesion by Microscale Topographical Cues. *Small* **2008**, *4*, 1416–1424.

6. Raimondi, M. T.; Eaton, S. M.; Laganà, M.; Aprile, V.; Nava, M. M.; Cerullo, G.; Osellame, R. Three-Dimensional Structural Niches Engineered *via* Two-Photon Laser Polymerization Promote Stem Cell Homing. *Acta Biomater.* **2013**, *9*, 4579–4584.

7. Kuo, S.-W.; Lin, H.-I.; Ho, J. H.; Shih, Y.-R. V.; Chen, H.-F.; Yen, T.-J.; Lee, O. K. Regulation of the Fate of Human Mesenchymal Stem Cells by Mechanical and Stereo-Topographical Cues Provided by Silicon Nanowires. *Biomaterials* **2012**, *33*, 5013–5022.

8. Downing, T. L.; Soto, J.; Morez, C.; Houssin, T.; Fritz, A.; Yuan, F.; Chu, J.; Patel, S.; Schaffer, D. V.; Li, S. Biophysical Regulation of Epigenetic State and Cell Reprogramming. *Nat. Mater.* **2013**, *12*, 1154–1162.

9. Lim, J. Y.; Donahue, H. J. Cell Sensing and Response to Micro- and Nanostructured Surfaces Produced by Chemical and Topographic Patterning. *Tissue Eng.* **2007**, *13*, 1879–1891.

10. Nikkhah, M.; Edalat, F.; Manoucheri, S.; Khademhosseini, A. Engineering Microscale Topographies to Control the Cell−substrate Interface. *Biomaterials* **2012**, *33*, 5230–5246.

11. Yang, Y.; Leong, K. W. Nanoscale Surfacing for Regenerative Medicine. *Wiley Interdiscip. Rev.: Nanomed. Nanobiotechnol.* **2010**, *2*, 478–495.

12. Chen, W.; Villa-Diaz, L. G.; Sun, Y.; Weng, S.; Kim, J. K.; Lam, R. H. W.; Han, L.; Fan, R.; Krebsbach, P. H.; Fu, J. Nanotopography Influences Adhesion, Spreading, and Self-Renewal of Human Embryonic Stem Cells. *ACS Nano* **2012**, *6*, 4094–4103.

13. Teo, B. K. K.; Wong, S. T.; Lim, C. K.; Kung, T. Y. S.; Yap, C. H.; Ramagopal, Y.; Romer, L. H.; Yim, E. K. F. Nanotopography Modulates Mechanotransduction of Stem Cells and Induces Differentiation through Focal Adhesion Kinase. *ACS Nano* **2013**, *7*, 4785–4798.

14. Sjöström, T.; Dalby, M. J.; Hart, A.; Tare, R.; Oreffo, R. O. C.; Su, B. Fabrication of Pillar-like Titania Nanostructures on Titanium and Their Interactions with Human Skeletal Stem Cells. *Acta Biomater.* **2009**, *5*, 1433–1441.

15. Watari, S.; Hayashi, K.; Wood, J. A.; Russell, P.; Nealey, P. F.; Murphy, C. J.; Genetos, D. C. Modulation of Osteogenic Differentiation in hMSCs Cells by Submicron Topographically-Patterned Ridges and Grooves. *Biomaterials* **2012**, *33*, 128–136.

16. Marino, A.; Ciofani, G.; Filippeschi, C.; Pellegrino, M.; Pellegrini, M.; Orsini, P.; Pasqualetti, M.; Mattoli, V.; Mazzolai, B. Two-Photon Polymerization of Sub-Micrometric Patterned Surfaces: Investigation of Cell-Substrate Interactions and Improved Differentiation of Neuron-like Cells. *ACS Appl. Mater. Interfaces* **2013**, *5*, 13012–13021.

17. Tonazzini, I.; Pellegrini, M.; Pellegrino, M.; Cecchini, M. Interaction of Leech Neurons with Topographical Gratings: Comparison with Rodent and Human Neuronal Lines and Primary Cells. *Interface Focus* **2013**, *4*, 20130047–20130047.

18. Bosman, F. T.; Stamenkovic, I. Functional Structure and Composition of the Extracellular Matrix. *J. Pathol.* **2003**, *200*, 423–428.

19. Díaz Lantada, A.; Pareja Sánchez, B.; Gómez Murillo, C.; Urbieta Sotillo, J. Fractals in Tissue Engineering: Toward Biomimetic Cell-Culture Matrices, Microsystems and Microstructured Implants. *Expert Rev. Med. Devices* **2013**, *10*, 629–648.

20. Lantada, A. D.; Morgado, P. L.; Otero, J. E.; Tanarro, E. C.; Ochoa, E. de la, G.; Munoz-Guijosa, J. M.; Sanz, J. L. M. In *Biomimetic Computer-Aided Design and Manufacture of Biological Surfaces*. Proceedings of the International Conference on Biomedical Electronics and Devices, Vilamoura, Algarve; Portugal, Feb 1–4, 2012; Fernandez-Chimeno, M., Solé-Casals, J., Fred, A. L. N., Gamboa, H., Eds.; SciTePress: Lisbon, 2012.

21. Bianchi, F.; Rosi, M.; Vozzi, G.; Emanueli, C.; Madeddu, P.; Ahluwalia, A. Microfabrication of Fractal Polymeric Structures for Capillary Morphogenesis: Applications in Therapeutic Angiogenesis and in the Engineering of Vascularized Tissue. *J. Biomed. Mater. Res., Part B* **2007**, *81B*, 462–468.

22. Schwartz Fo, H. O.; Novaes, A. B.; De Castro, L. M. S.; Rosa, A. L.; De Oliveira, P. T. *In Vitro* Osteogenesis on a Microstructured Titanium Surface with Additional Submicron-Scale Topography. *Clin. Oral Implants Res.* **2007**, *18*, 333–344.

23. Tonazzini, I.; Bystrenova, E.; Chelli, B.; Greco, P.; Stoliar, P.; Calò, A.; Lazar, A.; Borgatti, F.; D'Angelo, P.; Martini, C.; *et al.* Multiscale Morphology of Organic Semiconductor Thin Films Controls the Adhesion and Viability of Human Neural Cells. *Biophys. J.* **2010**, *98*, 2804–2812.

24. Díaz-Lantada, A.; Mosquera, A.; Endrino, J. L.; Lafont, P. Design and Rapid Prototyping of DLC Coated Fractal Surfaces for Tissue Engineering Applications. *J. Phys. Conf. Ser.* **2010**, *252*, 012003.

25. Kumar, G.; Waters, M. S.; Farooque, T. M.; Young, M. F.; Simon, C. G., Jr. Freeform Fabricated Scaffolds with Roughened Struts That Enhance Both Stem Cell Proliferation and Differentiation by Controlling Cell Shape. *Biomaterials* **2012**, *33*, 4022–4030.

26. Dalby, M. J.; Gadegaard, N.; Tare, R.; Andar, A.; Riehle, M. O.; Herzyk, P.; Wilkinson, C. D. W.; Oreffo, R. O. C. The Control of Human Mesenchymal Cell Differentiation Using Nanoscale Symmetry and Disorder. *Nat. Mater.* **2007**, *6*, 997–1003.

27. Degidi, M.; Iezzi, G.; Piattelli, A.; Perrotti, V. Implant Surfaces and Fractals. *Identity* **2012**, *12*, 7–11.

28. Gentile, F.; Medda, R.; Cheng, L.; Battista, E.; Scopelliti, P. E.; Milani, P.; Cavalcanti-Adam, E. A.; Decuzzi, P. Selective Modulation of Cell Response on Engineered Fractal Silicon Substrates. *Sci. Rep.* **2013**, *3*, 1461.

29. Cumpston, B. H.; Ananthavel, S. P.; Barlow, S.; Dyer, D. L.; Ehrlich, J. E.; Erskine, L. L.; Heikal, A. A.; Kuebler, S. M.; Lee, I.-Y. S.; McCord-Maughon, D.; *et al.* Two-Photon Polymerization Initiators for Three-Dimensional Optical Data Storage and Microfabrication. *Nature* **1999**, *398*, 51–54.

30. Haske, W.; Chen, V. W.; Hales, J. M.; Dong, W.; Barlow, S.; Marder, S. R.; Perry, J. W. 65 nm Feature Sizes Using Visible Wavelength 3-D Multiphoton Lithography. *Opt. Express* **2007**, *15*, 3426.

31. Raimondi, M. T.; Eaton, S. M.; Nava, M. M.; Laganà, M.; Cerullo, G.; Osellame, R. Two-Photon Laser Polymerization: From Fundamentals to Biomedical Application in Tissue Engineering and Regenerative Medicine. *J. Appl. Biomater. Funct. Mater.* **2012**, *10*, 55–65.

32. Marino, A.; Filippeschi, C.; Genchi, G. G.; Mattoli, V.; Mazzolai, B.; Ciofani, G. The Osteoprint: A Bioinspired Two-Photon Polymerized 3-D Structure for the Enhancement of Bone-like Cell Differentiation. *Acta Biomater.* **2014**, *10*, 4303–4313.

33. Klein, F.; Striebel, T.; Fischer, J.; Jiang, Z.; Franz, C. M.; von Freymann, G.; Wegener, M.; Bastmeyer, M. Elastic Fully Three-Dimensional Microstructure Scaffolds for Cell Force Measurements. *Adv. Mater.* **2010**, *22*, 868–871.

34. Delignières, D.; Torre, K.; Bernard, P.-L. Transition from Persistent to Anti-Persistent Correlations in Postural Sway Indicates Velocity-Based Control. *PLoS Comput. Biol.* **2011**, *7*, e1001089.

35. P, M.; S, H.; R, M.; M, G.; W S, K. Adult Mesenchymal Stem Cells and Cell Surface Characterization—A Systematic Review of the Literature. *Open Orthop. J.* **2011**, *5*, 253–260.

36. Katoh, K.; Masuda, M.; Kano, Y.; Fujiwara, K.; Jinguji, Y. Focal Adhesion Proteins Associated with Apical Stress Fibers of Human Fibroblasts. *Cell Motil. Cytoskeleton* **1995**, *31*, 177–195.

37. Hirata, H.; Tatsumi, H.; Lim, C. T.; Sokabe, M. Force-Dependent Vinculin Binding to Talin in Live Cells: A Crucial Step in Anchoring the Actin Cytoskeleton to Focal Adhesions. *Am. J. Physiol.: Cell Physiol.* **2014**, *306*, C607–620.

38. Lyu, Z.; Wang, H.; Wang, Y.; Ding, K.; Liu, H.; Yuan, L.; Shi, X.; Wang, M.; Wang, Y.; Chen, H. Maintaining the Pluripotency of Mouse Embryonic Stem Cells on Gold Nanoparticle Layers with Nanoscale but Not Microscale Surface Roughness. *Nanoscale* **2014**, *6*, 6959–6969.

39. Chowdhury, F.; Li, Y.; Poh, Y.-C.; Yokohama-Tamaki, T.; Wang, N.; Tanaka, T. S. Soft Substrates Promote Homogeneous Self-Renewal of Embryonic Stem Cells *via* Downregulating Cell-Matrix Tractions. *PLoS One* **2010**, *5*, e15655.

40. Kiuchi, T.; Nagai, T.; Ohashi, K.; Mizuno, K. Measurements of Spatiotemporal Changes in G-Actin Concentration Reveal Its Effect on Stimulus-Induced Actin Assembly and Lamellipodium Extension. *J. Cell Biol.* **2011**, *193*, 365–380.

41. Dlugosz, J. A.; Munk, S.; Ispanovic, E.; Goldberg, H. J.; Whiteside, C. I. Mesangial Cell Filamentous Actin Disassembly and Hypocontractility in High Glucose Are Mediated by PKC-Z. *Am. J. Physiol.: Renal Physiol.* **2002**, *282*, F151–F163.

42. Pollard, T. D.; Blanchoin, L.; Mullins, R. D. Molecular Mechanisms Controlling Actin Filament Dynamics in Nonmuscle Cells. *Annu. Rev. Biophys. Biomol. Struct.* **2000**, *29*, 545–576.

43. Safer, D.; Nachmias, V. T. Beta Thymosins as Actin Binding Peptides. *BioEssays* **1994**, *16*, 473–479.

44. Carlier, M.-F.; Pantaloni, D. Control of Actin Assembly Dynamics in Cell Motility. *J. Biol. Chem.* **2007**, *282*, 23005–23009.

45. Gingras, A. R.; Ziegler, W. H.; Frank, R.; Barsukov, I. L.; Roberts, G. C. K.; Critchley, D. R.; Emsley, J. Mapping and Consensus Sequence Identification for Multiple Vinculin Binding Sites within the Talin Rod. *J. Biol. Chem.* **2005**, *280*, 37217–37224.

46. Pasapera, A. M.; Schneider, I. C.; Rericha, E.; Schlaepfer, D. D.; Waterman, C. M. Myosin II Activity Regulates Vinculin Recruitment to Focal Adhesions through FAK-Mediated Paxillin Phosphorylation. *J. Cell Biol.* **2010**, *188*, 877–890.

47. Oakes, P. W.; Beckham, Y.; Stricker, J.; Gardel, M. L. Tension is Required but not Sufficient for Focal Adhesion Maturation without a Stress Fiber Template. *J. Cell Biol.* **2012**, *196*, 363–374.

48. Marcoux, N.; Vuori, K. EGF Receptor Activity Is Essential for Adhesion-Induced Stress Fiber Formation and Cofilin Phosphorylation. *Cell. Signalling* **2005**, *17*, 1449–1455.

49. Chrzanowska-Wodnicka, M.; Burridge, K. Rho-Stimulated Contractility Drives the Formation of Stress Fibers and Focal Adhesions. *J. Cell Biol.* **1996**, *133*, 1403–1415.

50. Ridley, A. J.; Hall, A. The Small GTP-Binding Protein Rho Regulates the Assembly of Focal Adhesions and Actin Stress Fibers in Response to Growth Factors. *Cell* **1992**, *70*, 389–399.

51. Ingber, D. E.; Wang, N.; Stamenović, D. Tensegrity, Cellular Biophysics, and the Mechanics of Living Systems. *Rep. Prog. Phys.* **2014**, *77*, 046603.

52. Lecuit, T.; Lenne, P.-F. Cell Surface Mechanics and the Control of Cell Shape, Tissue Patterns and Morphogenesis. *Nat. Rev. Mol. Cell Biol.* **2007**, *8*, 633–644.

53. Gauthier, N. C.; Masters, T. A.; Sheetz, M. P. Mechanical Feedback between Membrane Tension and Dynamics. *Trends Cell Biol.* **2012**, *22*, 527–535.

54. McBeath, R.; Pirone, D. M.; Nelson, C. M.; Bhadriraju, K.; Chen, C. S. Cell Shape, Cytoskeletal Tension, and RhoA Regulate Stem Cell Lineage Commitment. *Dev. Cell* **2004**, *6*, 483–495.

55. Müller, P.; Langenbach, A.; Kaminski, A.; Rychly, J. Modulating the Actin Cytoskeleton Affects Mechanically Induced Signal Transduction and Differentiation in Mesenchymal Stem Cells. *PLoS One* **2013**, *8*, e71283.

56. Treiser, M. D.; Yang, E. H.; Gordonov, S.; Cohen, D. M.; Androulakis, I. P.; Kohn, J.; Chen, C. S.; Moghe, P. V. Cytoskeleton-Based Forecasting of Stem Cell Lineage Fates. *Proc. Natl. Acad. Sci. U.S.A.* **2010**, *107*, 610–615.

57. Wu, K.-C.; Tseng, C.-L.; Wu, C.-C.; Kao, F.-C.; Tu, Y.-K.; C So, E.; Wang, Y.-K. Nanotechnology in the Regulation of Stem Cell Behavior. *Sci. Technol. Adv. Mater.* **2013**, *14*, 054401.

58. Nečas, D.; Klapetek, P. Gwyddion: An Open-Source Software for SPM Data Analysis. *Cent. Eur. J. Phys.* **2012**, *10*, 181–188.

59. Anguiano, E.; Pancorbo, M.; Aguilar, M. Fractal Characterization by Frequency Analysis. I. Surfaces. *J. Microsc.* **1993**, *172*, 223–232.

60. Aguilar, M.; Anguiano, E.; Pancorbo, M. Fractal Characterization by Frequency Analysis. II. A New Method. *J. Microsc.* **1993**, *172*, 233–238.

61. Pancorbo, M.; Anguiano, E.; Aguilar, M. Fractal Characterization by Frequency Analysis: III. Effect of Noise. *J. Microsc.* **1994**, *176*, 54–62.

62. Gillespie, P. A. Self-Affine Fractals. In *Fractals and Chaos in Geology and Geophysics*; Turcotte, D. L., Ed.; Cambridge University Press: Cambridge, U.K, 1992.

63. Ollion, J.; Cochennec, J.; Loll, F.; Escudé, C.; Boudier, T. TANGO: A Generic Tool for High-Throughput 3D Image Analysis for Studying Nuclear Organization. *Bioinformatics* **2013**, *29*, 1840–1841.

64. Sánchez, D.; Johnson, N.; Li, C.; Novak, P.; Rheinlaender, J.; Zhang, Y.; Anand, U.; Anand, P.; Gorelik, J.; Frolenkov, G. I.; *et al.* Noncontact Measurement of the Local Mechanical Properties of Living Cells Using Pressure Applied *via* a Pipette. *Biophys. J.* **2008**, *95*, 3017–3027.

65. Pellegrino, M.; Pellegrini, M.; Orsini, P.; Tognoni, E.; Ascoli, C.; Baschieri, P.; Dinelli, F. Measuring the Elastic Properties of Living Cells through the Analysis of Current−Displacement Curves in Scanning Ion Conductance Microscopy. *Pfluegers Arch.* **2012**, *464*, 307–316.

66. Rheinlaender, J.; Schäffer, T. E. Mapping the Mechanical Stiffness of Live Cells with the Scanning Ion Conductance Microscope. *Soft Matter* **2013**, *9*, 3230.